# Journal of Materials Chemistry A

Accepted Manuscript


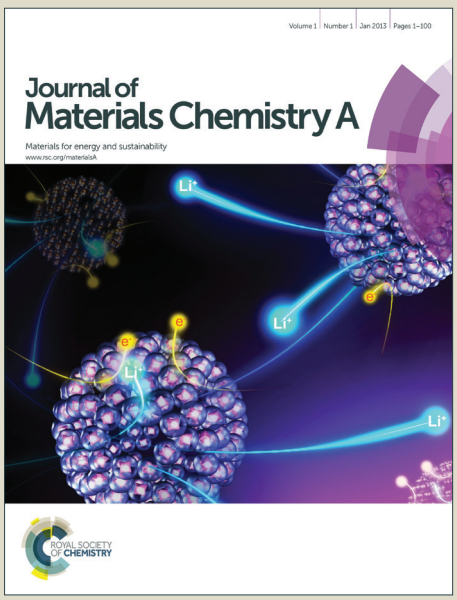





ROYAL SOCIETY OF CHEMISTRY

www.rsc.org/materialsA

Journal of Materials Chemistry A

Journal of Materials Chemistry A

Dynamic Article Links ►

Cite this: DOI: 10.1039/c0xx00000x

www.rsc.org/xxxxxx

**ARTICLE TYPE**

# *In situ* solution plasma synthesis of nitrogen-doped carbon nanoparticles as metal-free electrocatalysts for oxygen reduction reaction†

**Gasidit Panomsuwan,*[a] Satoshi Chiba,[a] Youta Kaneko,[a] Nagahiro Saito[b,c,d] and Takahiro Ishizaki[a,d]**

***Received (in XXX, XXX) Xth XXXXXXXXX 20XX, Accepted Xth XXXXXXXXX 20XX***
**DOI: 10.1039/b000000x**

We report the *in situ* synthesis of nitrogen-doped carbon nanoparticles (NCNPs) by solution plasma process without the addition of metal catalysts. Organic liquid mixtures of benzene and pyrazine were used as the precursor for the synthesis. The nitrogen-doping content can be controlled easily by changing the amount of pyrazine in the precursor. The synthesized NCNPs from solution plasma process exhibit a turbostratic structure with highly uniform nanoscale particles. The nitrogen atoms can be incorporated into the entire carbon structure homogeneously owing to the *in situ* doping during the growth and formation of carbon particles. The electrochemical activity toward oxygen reduction reaction (ORR) of NCNPs in an alkaline medium reveal the improvement in terms of both onset potential and current density as the nitrogen-doping content increases. The enhanced ORR activity of NCNPS is mainly attributed to the presence of pyridinic-N and graphitic-N bonding configurations. They also possess long-term durability and excellent tolerance to methanol crossover effects. The results obtained in this study have demonstrated that the solution plasma process has great potential for the synthesis of metal-free carbon-based ORR electrocatalysts. We expect that this approach can be extended to the further synthesis of other heteroatom-doped carbonaceous materials for a broad range of research activities in energy conversion and storage.

## 1. Introduction

The oxygen reduction reaction (ORR) is the most important electrochemical reaction occurring at the cathode in fuel cells, which can significantly limit their performance.[1] The Pt-based electrocatalysts have long been regarded as cathode materials in the fuel-cell technology because they are most catalytically active toward ORR.[2,3] However, high cost, limited supply, poor long-term durability, and electrochemical oxidation of carbon monoxide and methanol of Pt-based electrocatalysts are the major bottleneck for large-scale commercialization of fuel cells. It is therefore crucial to explore and develop the alternative electrocatalysts with highly efficient ORR activity and practical durability to replace the Pt-based electrocatalysts. Metal-free nitrogen-doped carbonaceous materials have been proposed as promising cathode materials for the next-generation fuel cells in the recent years.[4–8] Gong *et al*. reported that the vertically aligned nitrogen-doped carbon nanotube arrays exhibited superior ORR performance in terms of activity and stability to conventional Pt/carbon catalyst in an alkaline medium.[9] This finding presented the most important breakthrough in the catalysis research on metal-free electrocatalysts for fuel-cell cathode. Since then, the research in this exciting field has been rapidly growing and developing in a broad range of carbonaceous materials (e.g., mesoporous carbon, carbon nanocage, carbon nanofiber, grapheme, etc.) through various synthetic methods.[10–16]

Existing synthetic methods for preparation of nitrogen-doped carbonaceous materials have mostly relied on either *ex situ* doping through post treatment of pristine carbons or *in situ* doping during synthesis.[17] In the case of *ex situ* doping, the pristine carbons are heated at high temperature under the nitrogen atmosphere (e.g., ammonia, nitrogen plasma, etc.), which results in surface functionalization or edge-site doping with remaining their bulk properties.[18–21] On the other hand, the *in situ* doping can be performed by chemical vapor deposition (CVD) [22,23] or the pyrolysis of nitrogen containing hydrocarbons (e.g., acetonitrile, urea, melamine-formaldyhide, dicyandiamide, etc.).[24–27] These methods lead to the uniform incorporation of nitrogen atoms into the entire carbon frameworks. Although numerous efforts have been developed and achieved for the *in situ* synthesis of nitrogen-doped carbonaceous materials, the metal catalysts are inevitably required in the synthetic process and they are difficult to remove completely from the final products. Therefore, the exploration of a facile, efficient, scalable, and meat-catalyst-free synthetic pathway still remains a significant challenge. Recently, pulsed plasma in liquid, so called solution plasma process, has gained a noticeable attention for a wide variety of materials science and engineering, such as synthesis of metal and metal oxide

nanoparticles,[28–30] decomposition of biopolymer,[31] surface functionalization,[32] and synthesis of carbonaceous materials.[33–35] Solution plasma process offers several merits, such as simple experimental system, inexpensiveness, short-time operation, room-temperature processing, and atmospheric pressure.[36] These merits enable the solution plasma process to ultimately extend to the industrial scales of production and practical applications. Considering the synthesis of the carbonaceous materials by solution plasma process, various kinds of liquid organic solvents have been used as precursors for the synthesis, such as benzene, toluene, *n*-hexane, ethanol, etc.[33,37,38] The question has been raised: can solution plasma process apply for the *in situ* synthesis of nitrogen-doped carbonaceous materials? Up to the present time, the nitrogen-doped carbonaceous materials synthesized by solution plasma process are in the nascent stage and still questionable for the electrocatalysis community. Therefore, a deeper understanding of their physico-chemical properties as well as electrocatalytic activity is highly required in order to provide a strong basis for the future development in this field.

In this study, the nitrogen-doped carbon nanoparticles (NCNPs) were *in situ* synthesized by solution plasma process using the organic mixtures of benzene and pyrazine as the precursors without addition of metal catalysts. Pyrazine, a six membered-aromatic molecule containing two nitrogen atoms at two opposite ends of the aromatic ring, was used as a nitrogen source (Fig. 1). The nitrogen-doping content in NCNPs was adjusted by varying the amount of pyrazine in the organic mixtures. The physico-chemical properties and the electrocatalytic activity toward ORR in an alkaline medium of NCNPs were investigated and discussed comprehensively.

## 2. Experimental section

### 2.1 Chemicals

Benzene ($C_6H_6$, purity 99.5%), ethanol ($C_2H_5OH$, purity 99.5%), methanol ($CH_3OH$, purity 99.8%), and 0.1 M potassium hydroxide (KOH) aqueous solution were obtained from Kanto Chemical Co., Inc. Nafion®117 solution (5% w/v in a mixture of low molecular weight alcohols) and 20 wt% Pt on Vulcan XC-72 (20% Pt/C) were obtained from Sigma-Aldrich. Pyrazine ($C_4H_4N_2$, purity 98.0%) was obtained from Tokyo Chemical Industry. All reagents were of analytical reagent grade and used without further purification. Ultrapure water (18.2 MΩ·cm at 25 °C) was obtained by purification with an Advantec RFD 250NB system and used throughout all experiments.

### 2.2 Synthesis of nitrogen-doped carbon nanoparticles

Figure 1 depicts the schematic illustration of solution plasma process setup used for synthesizing NCNPs in this study. The 1 mm-diameter tungsten wire (purity 99.9%, Nilaco Corporation) was used as the electrode, which were shielded with an insulating ceramic tube. A pair of tungsten electrodes was placed at the center of a glass reactor with a gap distance of 1.0 mm. A bipolar high voltage pulse of. 1.5 kV was applied to the tungsten electrodes using a Pekuris MPP-HV04 high-voltage bipolar pulse generator. The pulse duration and pulse repetition frequency were fixed at 1 μs and 20 kHz, respectively. The organic mixtures of benzene and pyrazine were used as the precursors for the synthesis. The amount of nitrogen-doping content was adjusted

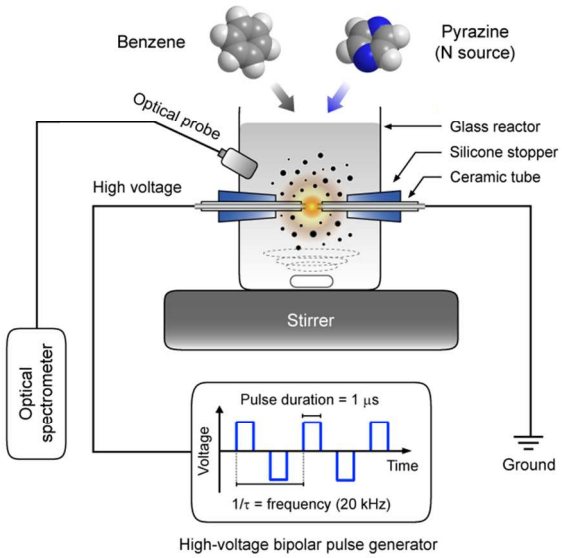


**Fig. 1** Schematic illustration of the experimental setup for solution plasma synthesis of NCNPs in this study.

by varying volume ratio between benzene and pyrazine as 70:30, 50:50 and 30:70. Plasma was initiated and stably maintained in 100 mL of the mixed organic precursors under vigorous stirring for 20 min. Once the plasma was generated at the gap between electrodes, the formation of carbon particles can be readily observed. After synthesis, the carbon particles were separated by filtration, followed by repeatedly washing with ethanol in order to remove soluble organic compounds. As-synthesized NCNPs were then dried at 60 °C for 12 h. The dried NCNPs were ground uniformly prior to thermally anneal in a quartz tube furnace at 800 °C for 2 h with a heating rate of 5 °C $min^{-1}$ under the Ar flow rate of 0.5 L $min^{-1}$. The NCNPs synthesized from the organic mixtures of benzene and pyrazine with the ratio of 70:30, 50:50, and 30:70 are hereafter designated as NCNP-30, NCNP-50, and NCNP-70, respectively. The undoped carbon nanoparticles were also synthesized using pure benzene with the same procedure (hereafter designated as CNP) and concurrently investigated throughout this study for comparison. The yields of CNP, NCNP-30, NCNP-50, and NCNP-70 after discharge for 20 min are found to be about 410, 330, 296, and 240 mg, respectively.

### 2.3 Optical emission spectroscopy measurement

Optical emission spectroscopy (OES) of the plasma generated in benzene and the mixture of benzene and pyrazine were collected with an Avantes AvaSpec-3648 optical spectrometer at the initial stage of discharge in the wavelength range of 300–900 nm. Each spectrum was recorded by averaging 10 scans with a 200 ms integration time. The optical probe was set at the position of 15 mm above from the plasma zone.

### 2.4 Characterizations

Field-emission scanning electron microscopy (FE-SEM) images were taken on a JEOL JSM-7100F microscope at an accelerating voltage of 15 kV. Transmission electron microscopy (TEM) images, selected area electron diffraction (SAED), and energy dispersive spectroscopy (EDS) elemental mapping were acquired on a JEOL JEM-2500SE at an accelerating voltage of 200 kV.

Elemental analysis of C, H, and N was performed on a Perkin Elmer 2400 Series II CHNS/O elemental analyzer. Phase structure was identified using a Rigaku Ultima IV X-ray diffractometer with a monochromatic Cu K$\alpha$ radiation ($\lambda$ = 0.15418 nm) operating at 40 kV and 40 mA (1.6 kW). Raman spectroscopy data were recorded on a JASCO NRS-5100 Raman spectrometer equipped with a laser-excitation wavelength of 532.1 nm. X-ray photoelectron spectroscopy (XPS) measurements were carried out on a JEOL JPS-9010MC using a monochromatic Mg K$\alpha$ X-ray source (1253.6 eV). The emission current and anode voltage were operated at 25 mA and 10 kV, respectively. The binding energy was calibrated using C 1s peak (284.5 eV). The relevant fitting curves were analyzed by Gaussian line shape and Shirley background subtraction.

### 2.5 Electrochemical measurements

The catalyst ink for electrochemical measurements was prepared by dispersing 5 mg of finely ground catalyst in a mixture containing 480 μL of ultrapure water, 480 μL of ethanol, and 40 μL of Nafion®117 solution by ultrasonication for 30 min to obtain homogeneous dispersion. A total of 3 μL of a well-dispersed catalyst ink was applied onto a freshly polished glassy carbon (GC) disk electrode (diameter: 3 mm), yielding an approximate catalyst loading of 212 μg cm$^{-2}$, for cyclic voltammetry (CV) and chronoamperometry measurements. Linear sweep voltammetry (LSV) measurement was performed on a rotating ring-disk electrode (RRDE). A total of 5 μL of catalyst ink was applied onto a GC disk electrode (diameter: 4 mm) surrounded by a Pt ring (inner/outer-ring diameter: 5.0/7.0 mm), yielding an approximate catalyst loading of 199 μg cm$^{-2}$. They were then left to dry in air at room temperature for 6 h prior to measurement. The 20% Pt/C catalyst was also prepared under the same procedure for the comparison. All electrochemical measurements were performed on a computer-controlled ALS-CH model 704ES electrochemical analyzer (CH instrument Inc.) with a typical three-electrode system in 0.1 M KOH solutions at room temperature. Platinum coil and Ag/AgCl (saturated KCl) were used as counter and reference electrodes, respectively. The electrolyte was purged with high purity nitrogen or oxygen with a constant flow rate of 50 mL min$^{-1}$ for at least 30 min prior to each measurement.

## 3. Results and discussion

### 3.1 Morphology

A typical FE-SEM image of NCNP-70 in Fig. 2a clearly shows agglomerates of uniform nano-sized carbon particles with three-dimensionally interconnected structure. More detailed information on the morphology was obtained from the TEM investigation. Fig 2b and 2c display bright-field TEM images of NCNP-70. As can be seen, the carbon particles exhibit a ball-like shape with a diameter size in the range of *ca*. 15–40 nm (Fig. S1†). They are agglomerated with each other by coalescence of the surface forming chains, which can be explained by the diffusion limited aggregation (DLA) model.[33,39] A SAED pattern taken from the corresponding area in Fig. 2b consists of three

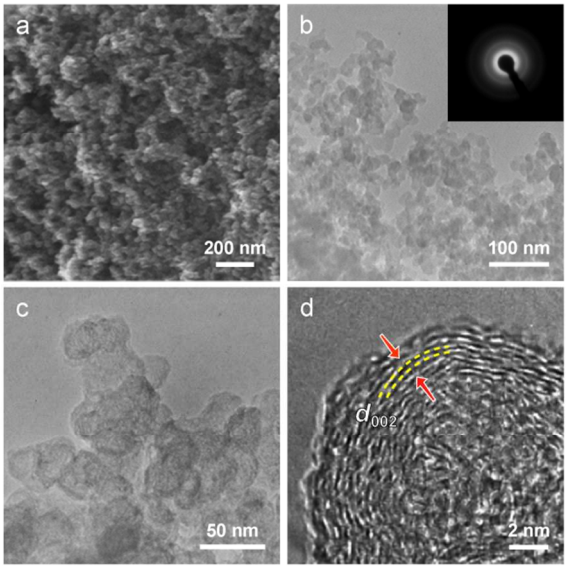


**Fig. 2** FE-SEM and TEM investigations on a representative NCNP-70: (a) FE-SEM image, (b,c) bright-field TEM images. A typical SAED pattern taken from the corresponding area in (b) is shown in the inset. (d) High-resolution TEM image.

diffused rings without any diffraction spots. The inner, middle, and outer diffraction rings represent correspond to (002), (100), and (101) planes of the turbostratic carbon structure, respectively.[40] It cannot be observed a significant change in the morphology and particle size with changing the amount of pyrazine in the precursors. From the high-resolution TEM images in Fig. 2d, the presence of lattice fringes corresponding to the (002) basal planes of turbostratic carbon are clearly visible. Such (002) basal planes are roughly parallel to each other to the edge of particles. The bending and interlinking between planes are also observed in some regions, indicating the disordered behavior in the carbon particles. The EDS elemental mapping was also

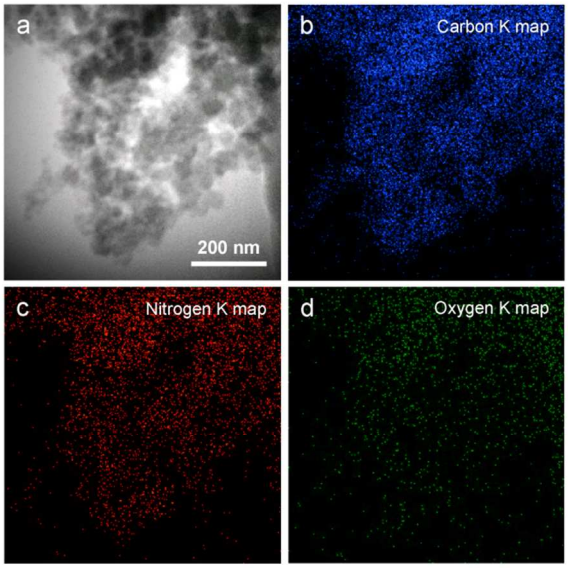


**Fig. 3** EDS elemental mapping of NCNP-70 taken from the area in (a) showing the distribution of (b) carbon, (c) nitrogen, and (d) oxygen.

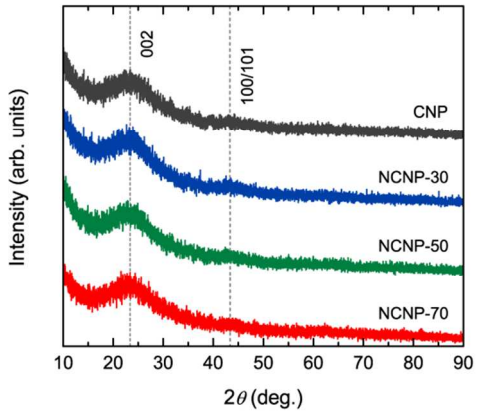


**Fig. 4** XRD patterns of CNP, NCNP-30, NCNP-50, and NCNP-70.

investigated on a relatively large area of NCNP-70 to confirm the presence of nitrogen atoms, as shown in Fig. 3. The NCNP-70 is composed of only carbon, oxygen, and nitrogen with highly homogeneous distribution throughout the investigated sample area. This result indicates that the nitrogen atoms can be incorporated into the carbon particles homogeneously. The quantitative analysis on the nitrogen-doping content in the carbon nanoparticles will be discussed below.

### 3.2 Structural properties

Structural information of CNP, NCNP-30, NCNP-50, and NCNP-70 were studied by XRD and Raman spectroscopy. The powder XRD patterns of all catalysts are revealed in Fig. 4. They exhibit similar diffraction characteristics, which are composed of a main broad peak at 23.5° and a small peak at 43.4° corresponding to the (002) and (100)/(101) planes of the carbon in turbostratic phase, respectively.[27,41] This result is in agreement with the aforementioned SAED pattern in previous section. The interlayer distance ($d_{002}$) of all catalysts is estimated to be about 0.3763 ± 0.003 nm, which is much larger than that of the ideal graphite (0.3354 nm). The expansion of $d_{002}$ is a common characteristic of disordered turbostratic phase, as reported elsewhere.[27,41,42] More insight into their structural properties was evaluated by Raman spectroscopy (Fig. 5). Two evident peaks are observed at 1598–1600 and 1350–1353 cm$^{-1}$ for all catalysts, which are

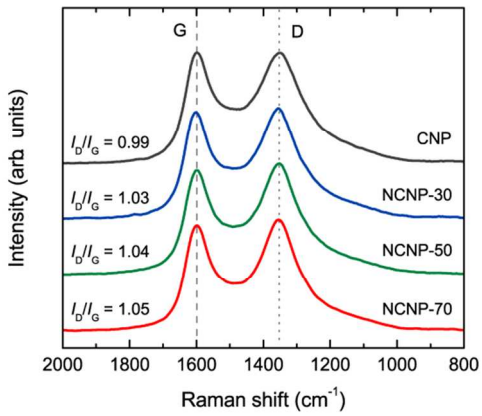


**Fig. 5** Raman spectra of the CNP, NCNP-30, NCNP-50, and NCNP-70. The vertical dashed and dotted lines are guides for the eyes to indicate the position of G- and D-bands, respectively.

**Table 1** Bulk and surface elemental composition of CNP, NCNP-30, NCNP-50, and NCNP-70 obtained from the EA and XPS measurements, respectively

| Catalyst | EA (wt%) | | | XPS (at%) | | |
|---|---|---|---|---|---|---|
| | C | H | N | C | O | N |
| CNP | 93.58 | 0.24 | - | 91.32 | 8.68 | - |
| NCNP-30 | 93.36 | 0.20 | 0.24 | 91.95 | 7.66 | 0.39 |
| NCNP-50 | 92.66 | 0.18 | 0.38 | 92.46 | 7.03 | 0.51 |
| NCNP-70 | 91.18 | 0.19 | 0.61 | 90.26 | 9.16 | 0.58 |

attributed to the G- and D-bands, respectively. The G-band refers to the graphitic $E_{2g}$ mode corresponding to the in-plane bond-stretching motion of the pair of sp$^2$ carbon atoms. On the other hand, the D-band is related to the breaking of symmetry caused by structural disorders and defects (e.g., lattice distortion, bond length disorder, vacancy, impurity, etc.).[43] Relative intensity ratio of the D-band to the G-band ($I_D/I_G$) is directly proportional to the amount of structural disorder in the carbon.[43,44] The $I_D/I_G$ is estimated to be 0.99, 1.03, 1.04, and 1.05 for the CNP, NCNP-30, NCNP-50, and NCNP-70, respectively. An increase in $I_D/I_G$ with increasing nitrogen-doping content suggests that the incorporation of nitrogen atoms into carbon structure can induce more defect sites and disordered structure.

### 3.3 Elemental composition and bonding configuration

The bulk elemental composition was examined by elemental analysis (EA). The amount of carbon, hydrogen, and nitrogen are listed in Table 1. The nitrogen-doping content is varied from 0.24 to 0.61 wt%, which is directly related to the amount of pyrazine in the mixed precursors. To further elaborate the surface elemental composition and bonding configuration of NCNPs, the XPS measurement was carried out. The XPS survey spectra of NCNPs show the major peaks corresponding to C 1s, N 1s and O 1s, whereas a significant peak from tungsten cannot be detected (Fig. S2†). This result confirms that the erosion of tungsten electrode during synthesis is negligible; therefore, the NCNPs synthesized from solution plasma process can be identified as metal-free catalysts. Surface elemental compositions of all catalysts can be quantitatively determined and summarized in Table 1. It is seen that the surface elemental composition determined from XPS measurement are consistent with the bulk elemental compositions obtained from EA. It may imply that the nitrogen atoms are incorporated into both bulk and surface of NCNPs homogeneously. High-resolution XPS C 1s spectra of all catalysts show the most pronounced peak of graphite-like carbon (C–C) at 284.5 eV (Fig. S3a†), indicating that most of carbon atoms are formed as sp$^2$ graphite structure. A long tail at higher binding energies is attributed to the carbon atoms attached to nitrogen and different oxygen-containing moieties (e.g., C–O, –O–C=O–, carbonate, etc.).[21,45] The presence of XPS O1s peak is possibly attributed to the oxidation of the carbon surface when exposed to the air condition (Fig. S3b†). The high-resolution XPS N 1s spectra of NCNP-30, NCNP-50, and NCNP-70 can be deconvoluted into four peaks (Fig. 6a and Fig. S3c†), including pyridinic-N ($N_P$: 398.4 ± 0.2 eV), pyrrolic-N ($N_{PR}$: 400.1 ± 0.2 eV), graphitic-N ($N_G$: 401.0 ± 0.1 eV), and pyridinic N-oxide ($N_{OX}$: 403.7 ± 0.1 eV).[6,10,46,47] Fig. 6b shows the nitrogen-doping

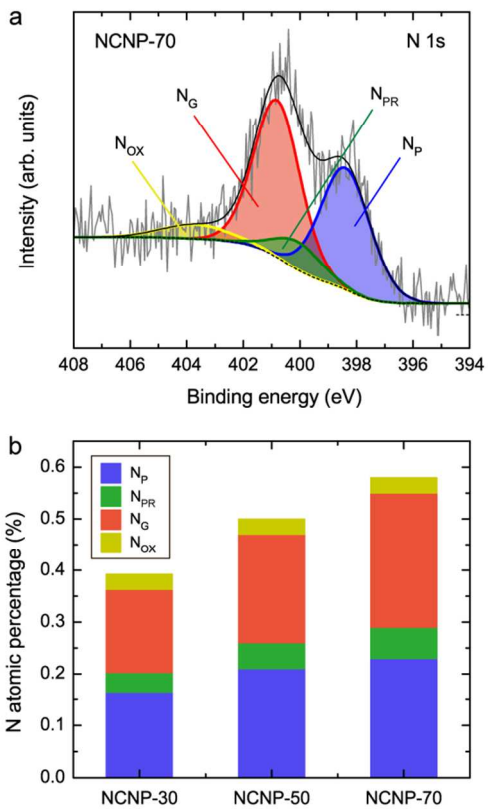


**Fig. 6** (a) High-resolution XPS N 1s spectra of NCNP-70. It can be deconvoluted into four peaks corresponding to four-type nitrogen bonding configurations, including pyridinic-N ($N_P$), pyrrolic-N ($N_{PR}$), graphitic-N ($N_G$), and pyridnic-N oxide ($N_{OX}$). (b) The relative atomic percentage of each nitrogen-bonding configuration of NCNP-30, NCNP-50, and NCNP-70.

content and relative amount of each nitrogen bonding configuration of NCNP-30, NCNP-50, and NCNP-70. It is found that the nitrogen-doping content increases from 0.39 at% for NCNP-30 to 0.58 at% for NCNP-70. The pyridinic-N (39–43%) and graphitic-N (42–46%) are the predominant bonding configurations on the surface of all NCNPs, whereas the amount of pyrrolic-N and pyridinic N-oxide are relatively lower (see Table S1†).

### 3.4 Electrocatalytic activity toward oxygen reduction reaction

The electrocatalytic activity toward ORR of all catalysts was first evaluated by CV measurements in 0.1 M KOH solution saturated with $N_2$ and $O_2$ at a scan rate of 50 mV $s^{-1}$ (Fig. S4†). In the $N_2$-saturated electrolyte, the featureless CV curves can clearly be observed. In contrast, the CV curves in an $O_2$-saturated electrolyte show the prominent cathodic peak corresponding to ORR for all catalysts, as revealed in Fig. 7. The onset potential and peak potential of ORR gradually shifts toward more positive potential as the nitrogen-doping content increases. Another important aspect is that the area under CV curve of NCNPs is slightly larger than that of CNP. This finding suggests that the nitrogen doping leads to a progressive enhancement of a specific surface area and its accessibility to the electrolyte. To gain more insight into the ORR performance of NCNPs, LSV measurements on a RRDE were carried out in an $O_2$-saturated 0.1 M KOH

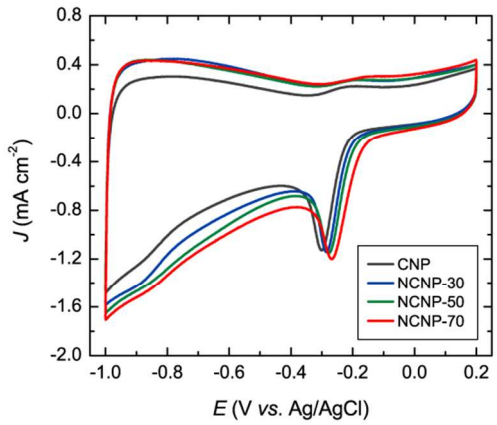


**Fig. 7** CV curves of ORR on CNP, NCNP-30, NCNP-50, and NCNP-70 modified GC-disk electrodes in an $O_2$-saturated 0.1 M KOH solution at a scan rate of 50 mV $s^{-1}$.

solution at a scan rate of 10 mV $s^{-1}$ and a rotation speed of 1600 rpm (Fig. 8a). The LSV curve of CNP exhibits two current plateaus with the onset potential at –0.22 and –0.67 V. Upon increasing the nitrogen-doping content, the onset potential of ORR positively shifts with a concomitant increase in current density, which is consistent with the results of CV measurement. The onset potential of NCNP-70 occurs at –0.17 V, which is 50 mV higher than that of CNP, followed by a continuous increase in the current density with no evident current plateau. A positive shift of the onset potential is pointed out that the ORR of NCNPs is more favorable than that of CNP. Although the NCNP-70 is catalytically most active for ORR among other catalysts, it is still inferior to a state-of-art commercial 20% Pt/C in terms of both onset potential and current density. The ORR process in an alkaline medium can occurs *via* two possible parallel reaction pathways: one is a direct four-electron pathway (Eqn (1)), in which $O_2$ can be directly reduced to $OH^-$ without the formation of $HO_2^-$ intermediate, and the other is a series of two-electron pathway (Eqn (2) and (3)), in which $O_2$ is firstly reduced to $HO_2^-$ intermediate followed by the subsequent reduction to $OH^-$.[8]

$$O_2 + H_2O + 4e^- \rightarrow 4OH^- \quad (1)$$

$$O_2 + H_2O + 2e^- \rightarrow HO_2^- + OH^- \quad (2)$$

$$HO_2^- + H_2O + 2e^- \rightarrow 3OH^- \quad (3)$$

It has been known that the formation of $HO_2^-$ in a two-electron pathway may lead to the deterioration of catalysts and fuel-cell performance owing to their high oxidizability. Therefore, the ORR occurring *via* a direct four-electron transfer pathway is much more desirable to render high-performance alkaline fuel cells. The ORR mechanisms catalyzed by all catalysts were evaluated by monitoring the formation of $HO_2^-$ intermediate during the ORR. The corresponding ring current density was measured with a Pt ring electrode by applying a constant potential of 0.5 V where $HO_2^-$ can be oxidized. It is seen that the ring current density is diminished with an increase in nitrogen-doping content, indicating the inhibition of $HO_2^-$ production from the ORR. The electron transfer number ($n$) per $O_2$ molecule involved in the ORR and the percentage of $O_2$ molecules that are reduced to $HO_2^-$ can be calculated on the basis of ring-disk currents by the following equations:[25,48]

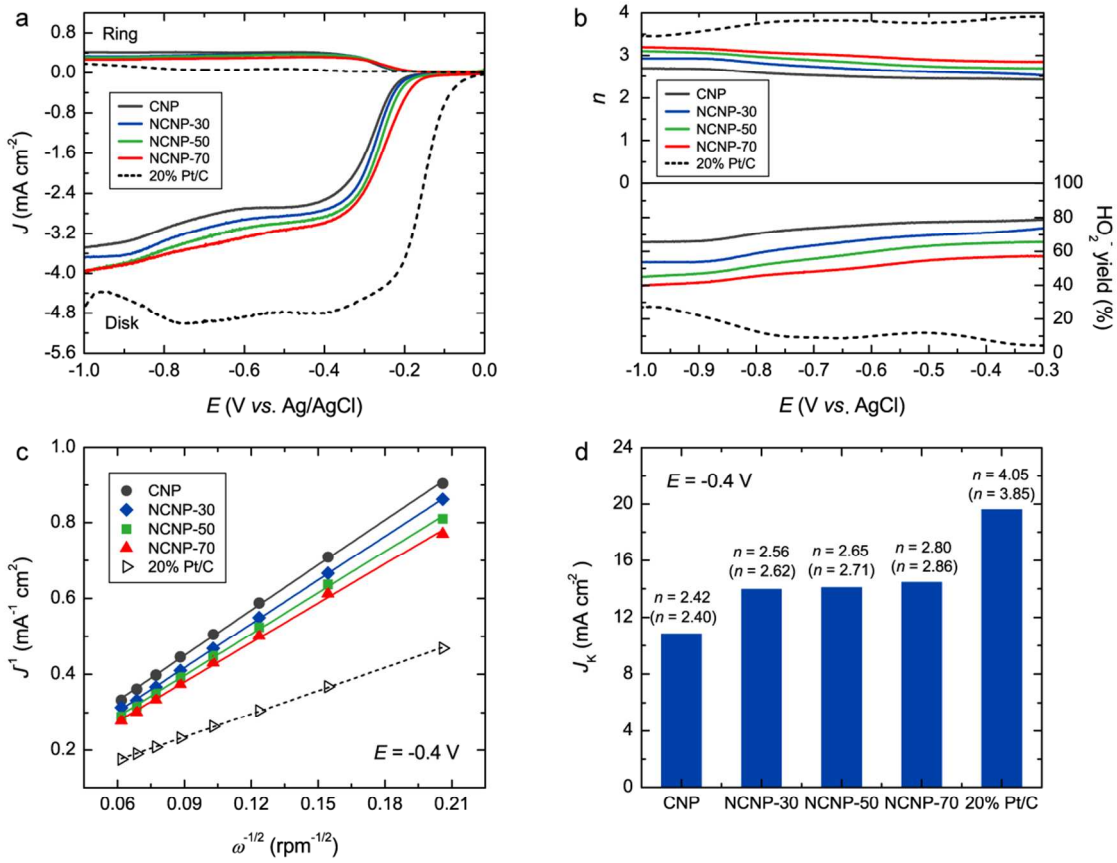


**Fig. 8** (a) LSV curves of all catalysts on a RRDE in an $O_2$-saturated 0.1 M KOH solution at a scan rate of 10 mV $s^{-1}$ and a rotation speed of 1600 rpm. A constant potential of 0.5 V was applied on the Pt ring electrode during the measurement. (b) The plots of electron transfer numbers ($n$) and $HO_2^-$ yields detected over all catalysts modified on GC-disk electrodes in the potential range from –0.3 to –1.0 V. (c) K–L plots of $J^{-1}$ versus $\omega^{-1/2}$ of all catalysts at a potential of –0.4 V obtained from LSV curves in an $O_2$-saturated 0.1 M KOH solution at a scan rate of 10 mV $s^{-1}$ with different rotation speeds from 225 to 2500 rpm (Fig. S5†). (d) Summary of $J_K$ and $n$ determined from the K–L analysis and RRDE data (values in parentheses) of all catalysts.

$$n = \frac{4 \times I_D}{I_D + I_R / N} \quad (4)$$

$$HO_2^-(\%) = 200 \times \frac{I_R / N}{I_D + I_R / N} \quad (5)$$

where $I_D$ is the disk current, $I_R$ is the ring current, and $N$ is the current collection efficiency of the Pt ring (0.37). The calculated $n$ values and $HO_2^-$ yield of all catalysts are plotted against the potentials from –0.3 to –1.0 V in Fig. 8b. The calculated $n$ values of 20% Pt/C are varied between 3.76 and 3.93 with low $HO_2^-$ yields over the potential range investigated. This result confirms that the ORR of 20%Pt/C proceeds *via* a dominantly direct four-electron pathway, in which $O_2$ is reduced directly to $OH^-$ following Eqn (1). In contrast, the calculated $n$ values of CNP are between 2.40 and 2.65, which are very close to that of bare GC electrode (Table S2†). This result indicates that the ORR of CNP mainly involves a two-electron pathway, resulting in $HO_2^-$ yield as high as 65–78%. As can be seen, the calculated $n$ values are found to gradually increase with a concomitant decrease of $HO_2^-$ yields throughout the potential range investigated as the nitrogen-doping content increases. The $n$ values of NCNP-70 are in the range of 2.84–3.20, implying that the ORR proceeds *via* parallel two- and four-electron pathways but the latter seems to be predominated at higher negative potential. Such higher $n$ values and lower $HO_2^-$ yields indicate that the nitrogen doping into carbon structure can inhibit the occurrence of a two-electron pathway and concurrently promote a four-electron pathway for the ORR in an alkaline medium. A series of LSVs curves of all catalysts in an $O_2$-saturated 0.1 M KOH solution at a different rotation speeds from 225 to 2500 rpm are demonstrated in Fig S5†. It is obvious that the current density of all catalysts progressively rises with an increase in the rotation speed. Based on the data above, the $n$ value can also be determined through the Koutecky–Levich (K–L) equations as follows:[49]

$$\frac{1}{J} = \frac{1}{J_K} + \frac{1}{J_D} = \frac{1}{J_K} + \frac{1}{B\omega^{1/2}} \quad (6)$$

$$B = 0.62nFD_O^{2/3}v^{-1/6}C_O \quad (7)$$

where $J$ is the measured current density, $J_K$ is the kinetic current density, $J_D$ is the diffusion current density, $\omega$ is the angular velocity of the disk ($\omega = 2\pi N$, $N$ is the linear rotation speed), $F$ is the Faraday constant (96485 C $mol^{-1}$), $D_O$ is the diffusion coefficient of $O_2$ ($1.73 \times 10^{-5}$ mol $L^{-1}$), $v$ is the kinematic viscosity of electrolyte (0.01 $cm^2$ $s^{-1}$), and $C_O$ is the bulk concentration of $O_2$ ($1.21\times 10^{-3}$ mol $L^{-1}$).[20,46] The K–L plots of the inverse of current density ($J^{-1}$) against the inverse of the square root of angular velocity ($\omega^{-1/2}$) of all catalysts at a

potential of –0.4 V are presented in Fig. 8c. The K–L plots display good linearity and their slopes remain approximately constant over the potential range from –0.4 to –0.6 V (Fig. S6†), indicating the first-order reaction kinetics with respect to oxygen species.[50] The slope of K–L plots becomes less steep with increasing nitrogen-doping content, implying an increase in *n* value. The ORR performance was also quantitatively evaluated in term of $J_K$ from the intercept of the linearly fitted K–L plot at a potential of –0.4 V. The calculated $J_K$ values with the corresponding *n* values obtained from the RRDE and K–L analysis are summarized in Fig. 8d. It can be seen that $J_K$ increases from 10.8 mA cm$^{-2}$ for CNP to 14.5 mA cm$^{-2}$ for NCNP-70 at a potential of –0.4 V. The *n* values of all catalysts calculated from the slope of K–L plots are consistent with those calculated from the RRDE method. It can be concluded that the incorporation of nitrogen atoms into graphitic carbon framework leads to the improvement of both the ORR performance and selectivity toward a four-electron pathway in an alkaline medium.

The improvement of ORR performance in NCNPs can be attributed to the creation of a net positive charge on the adjacent carbon atoms in the graphitic structure due to the higher electronegativity of nitrogen ($\chi_N$ = 3.0) when compared to that of carbon ($\chi_C$ = 2.55). The nitrogen-induced charge localization results in the change in chemisorption mode of $O_2$ from the usual end-on mode (Pauling model) to the diatomic side-on mode (Yeager model).[9] The $O_2$ molecules adsorbed on the active sites of the carbon by the side-on mode tend to release OH– by breaking the O–O bond of the $O_2$ molecules, thus catalyzing the ORR in a four-electron pathway. On the other hand, the $O_2$ molecule adsorbed on the active sites of the carbon by the end-on mode is predominantly reduced through a two-electron pathway to produce $HO_2^-$.[9,51,52] This means that the nitrogen doping would effectively weaken the O–O bonding and consequently facilitate the ORR process. Apart from the change in atomic charge distribution, Zhang *et al* reported that the spin density distribution is also important in inducing the catalytic active sites on the nitrogen-doped graphene according to the density functional theory (DFT) calculation.[53] Therefore, the disturbance of atomic charge and spin density distributions in the carbon structure by doping nitrogen atoms play the crucial roles in explaining why doping nitrogen atoms in the graphitic carbon framework can enhance the ORR activity.

Furthermore, it has been reported that the total nitrogen-doping content in the carbonaceous materials does not have a direct correlation with the improvement of ORR activity.[46] Only pyridinic-N and graphitic-N have been extensively proved as the important species in significantly enhancing limiting current and higher onset potential of ORR process in an alkaline medium, respectively.[21,46,47] On the other hand, the pyrrolic-N and pyridinic-N oxide seem to be unrelated and negligible to the ORR process. As discussed in the XPS measurements, the nitrogen bonding configurations on the surface of NCNPs are dominated by pyridinic-N and graphitic-N. Therefore, the enhancement in ORR activity of NCNPs in this study should be attributed to the presence of pyridinic-N and graphitic-N. However, the nitrogen-doping content of NCNPs in our study is relatively lower when compared to the several previous reports (see Ref. 6 and the references therein). To further improve both limiting current and onset potential for ORR, the synthesis of the NCNPs using other organic liquids containing more nitrogen atoms is still underway.

The major concerns of catalysts for current fuel-cell technology are their durability under long-term operation and the tolerance to the methanol crossover effect. Current–time (*I–t*) chronoamperometric response was performed at a constant potential of –0.4 V for 40000 s in an $O_2$-saturated 0.1 M KOH with a rotation speed of 1600 rpm to confirm the durability of NCNPs. As revealed in Fig. 9a, the relative current ($I/I_0$) of NCNP-70 exhibits a very slow attenuation with a remaining high relative current of about 85% after 40000 s, respectively. In contrast, the relative current of 20% Pt/C remarkably decreases to about 71% after 40000 s. This result confirms that the NCNP-70 has a much better long-term durability in an alkaline medium than 20% Pt/C. To further assess the tolerance to methanol crossover effect, 3M methanol was introduced into an $O_2$-saturated 0.1 M KOH solution during the *I–t* chronoamperrometric measurement at 1200 s (Fig. 9b). Once the 3M methanol was introduced, the current of 20% Pt/C abruptly drops about 10%, whereas that of NCNP-70 still remains unchanged and stable without degradation. This result is evidence that the NCNP-70 exhibits superior tolerance to the methanol crossover effect to 20% Pt/C. Fig. S8† demonstrates the CV curves of NCNP-70 and 20% Pt/C before and after the addition of 3M methanol. It can be seen that the electro-oxidation of methanol seriously degrade the ORR of 20% Pt/C, whereas the ORR of NCNP-70 remains almost unchanged.

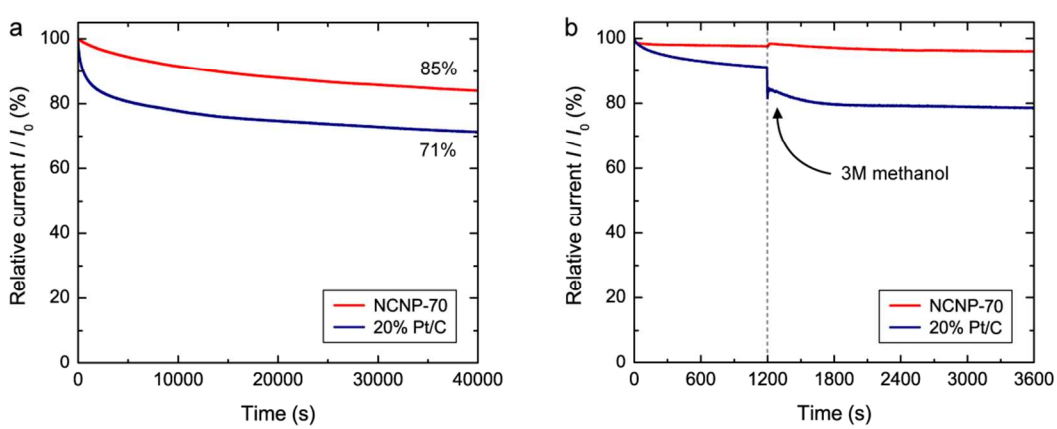


**Fig. 9** Durability test of NCNP-70 and 20% Pt/C: (a) *I–t* chronoamperometric response (1600 rpm) at –0.4 V in an $O_2$-saturated 0.1 M KOH solution for 40000 s. (b) *I–t* chronoamperometric responses (1600 rpm) with the addition of 3M methanol at 1200 s.

Cite this: DOI: 10.1039/c0xx00000x

www.rsc.org/xxxxxx

**ARTICLE TYPE**

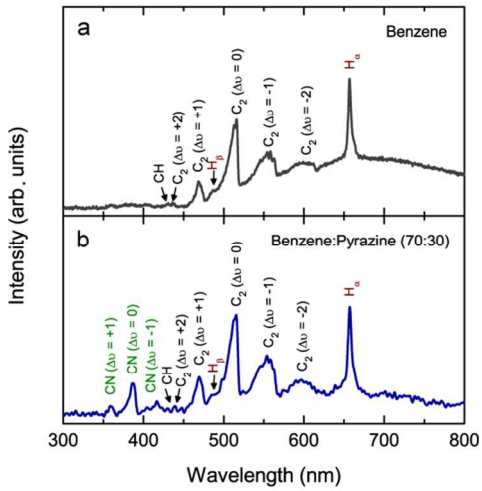


**Fig. 10** OES spectra recorded from the plasma generated in (a) pure benzene and (b) mixture of benzene and pyrazine (30:70).

### 3.4 Formation mechanism of NCNPs by solution plasma

To elucidate the formation mechanism of NCNPs, the OES spectra were recorded from the plasma generated in the benzene and the mixture of benzene and pyrazine, as revealed in Fig. 10a and 10b, respectively. Both the OES spectra show the dominant emission of Swan bands originated from diatomic carbon molecule ($C_2$) (transition $d^3\Pi_g \rightarrow a^3\Pi_u$; sequences $\Delta\upsilon = -2, -1, 0, +1, +2$) at the wavelength range of 432–630 nm.[54,55] It has been known that the $C_2$ radicals are the important species for the formation and growth of carbon materials.[33,38,55,56] In fact, the emission peak from CH radicals (transition $A^2\Delta \rightarrow X^2\Pi$) should be detected at 431 nm. However, it is difficult to see due to its very low intensity, which is consistent with several previous reports.[57–59] The emission peak at 487 and 696 nm are associated to Balmer atomic hydrogen $H_\beta$ and $H_\alpha$, respectively. This indicates the abstraction of hydrogen atoms from benzene and pyrazine molecules. For the mixture of benzene and pyrazine, in addition to the emission peaks from $C_2$, CH, and H radicals, it can also be observed the emission peaks attributed to CN violet system (transition $B^2\Sigma^+ \rightarrow X^2\Sigma^+$ sequence $\Delta\upsilon = -1, 0, +1$) at the shorter wavelengths from 350 to 420 nm.[55,57] Based the analysis of OES data, it can be suggested that the benzene molecules are first broken *via* ring-opening reactions due to high electron density and temperature (>3000 K) in plasma region. The open ring structures are subsequently decomposed into $C_2$, CH, and H radicals. The decomposition of pyrazine molecules should be explained by the same manner with that of benzene molecules, but they undergo more complex and multi-step dissociation.[60] The most important species from the decomposition of pyrazine is highly active CN radicals, which is a key factor for the nitrogen doping in carbon materials.[55,57–59] The highly reactive CN radicals can further react with $C_2$, CH, and H radicals. This can thus lead to the incorporation of nitrogen atoms at the first stage of the growth and formation of graphitic planes, which eventually form to the carbon particles with uniform nitrogen doping.

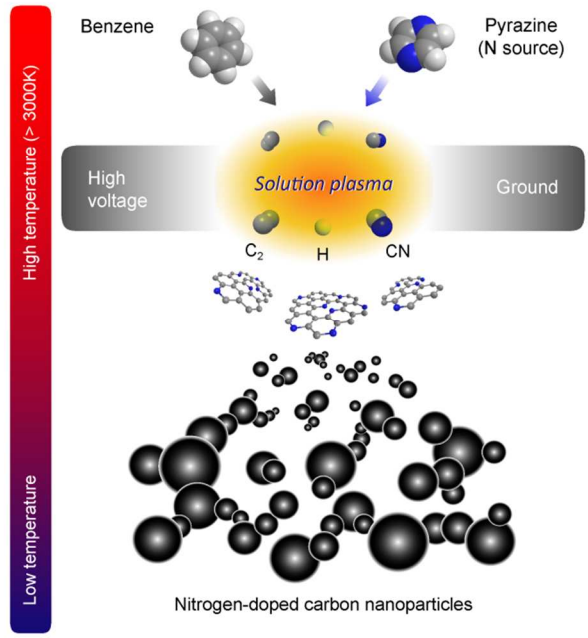


**Fig. 11** Schematic illustration of the growth and formation of NCNPs by solution plasma process.

Subsequently, the carbon particles are rapidly ejected from the plasma region to the liquid phase. Large temperature gradient between plasma and liquid phases results in a dramatic quenching of carbon particles, causing the freeze of their disorder structure. The schematic illustration of the formation of NCNPs is depicted in Fig. 11.

## 4. Conclusion

We have shed new light on the new synthetic route of NCNPs by solution plasma process from the mixture of benzene and pyrazine. The $C_2$ and CN radicals generated in the solution plasma under the presence of benzene and pyrazine molecules are the important species for the formation of NCNPs with *in situ* nitrogen doping throughout the structure. The nitrogen-doping content can be easily tuned by changing the amount of pyrazine in the mixed precursor. The NCNPs exhibit a turbostratic phase with a uniform nano-sized particle. For the electrochemical measurements in an alkaline medium, the ORR performance in terms of onset potential and current density are found to be improved as the nitrogen-doping content increases. The nitrogen doping can inhibit the occurrence of a two-electron pathway and concurrently promote a four-electron pathway for the ORR. The NCNPs also exhibit long-term durability and excellent tolerance to crossover effects of methanol for ORR when compared to commercial 20% Pt/C. The solution plasma process can be potentially extended to the synthesis of other heteroatoms-doped carbon nanoparticles (e.g., boron, phosphorus, sulfur and their mixtures) simply by changing the organic precursors. We believe that the further development through solution plasma process in

this exciting field will facilitate and accelerate the applications of metal-free ORR electrocatalysts for a broad range of advanced energy conversion and storage devices.

[a] *Department of Materials Science and Engineering, Faculty of Engineering, Shibaura Institute of Technology, Tokyo 135-8548, Japan. E-mail:i036050@sic.shibaura-it.ac.jp, g.panomsuwan@gmail.com; Fax: +81-34-859-8101; Tel: +81-3-5859-8115*

[b] *Department of Materials, Physics and Energy Engineering, Graduate School of Engineering, Nagoya University, Nagoya 464-8603, Japan.*

[c] *Green Mobility Collaborative Research Center, Nagoya University, Nagoya 464-8603, Japan*

[d] *Core Research for Evolutional Science and Technology (CREST), Japan Science and Technology Agency (JST), Saitama 333-0012, Japan.*

† Electronic Supplementary Information (ESI) available: survey XPS spectra, high-resoltuion XPS C 1s, O 1s, and N 1s spectra, CV curves measured in $N_2$- and $O_2$-saturated 0.1 KOH solutions, LSV curves at different rotation speeds, K–L plots derived, CV curves of NCNP-70 and 20% Pt/C in an $O_2$-saturated 0.1 KOH solution with and without 3M methanol. See DOI: 10.1039/b000000x/

## Notes and references

1 A. Rabis, P. Rodriguez and T. J. Schmidt, *ACS Catal*. 2012, **2**, 864.
2 Y. Bing, H. Liu, L. Zhang, D. Ghosh and J. Zhang, *Chem. Soc. Rev.*, 2010, **39**, 2184.
3 X. Zhao, M. Yin, L. Ma, L. Liang, C. Liu, J. Liao, T. Lu and Q. Xing, *Energy Environ. Sci*., 2011, **4**, 2736.
4 H. Wang, T. Maiyalagan and X. Wang, *ACS Catal*. 2012, **2**, 781.
5 J. P. Paraknowitsh and A. Thomas, *Energy Environ. Sci*., 2013, **6**, 2839.
6 N. Daems, X. Sheng, I. F. J. Vankelecom and P. P. Pescamona, *J. Mater. Chem. A*, 2014, **2**, 4085.
7 K. N. Wood, R. O'Hayre and S. Pylypenko, *Energy Environ. Sci*., 2014, **7**, 1212.
8 D.-W. Wang and D. Su, *Energy Environ. Sci*., 2014, **7**, 576.
9 K. Gong, F. Du, Z. Xia, M. Durstock and L. Dai, *Science*, 2009, **323**, 760.
10 S. Chen, J. Bi, Y. Zhao, L. Yang, C. Zhang, Y. Ma, Q. Wu, X. Wang and Z. Hu, *Adv. Mater*. 2012, **24**, 5593.
11 C. Zhu and S. Dong, *Nanoscale*, 2013, **5**, 1753.
12 L. Qu, Y. Liu, J.-B. Baek and L. Dai, *ACS Nano*, 2010, **4**, 1321.
13 Y. Li, T. Li, M. Yao and S. Liu, *J. Mater. Chem*., 2012, **22**, 10911.
14 J. Yin, J. Yu, X. Zhou and W. Wu, *RSC Adv*., 2013, **3**, 15655.
15 H. T. Chung, J. H. Won and P. Zelenay, *Nat. Commun*., 2013, **4**, 1922.
16 L. Feng, Y. Yan and Y. Chen, L. Wang, *Energy Environ. Sci.*, 2011, **4**, 1892.
17 D. Yu, E. Nagalli, F. Du and L. Dai, *J. Phys. Chem. Lett*., 2010, **1**, 2165.
18 B. Guo, Q. Liu, E. Chen, H. Zhu, L. Fang and J. R. Gong, *Nano Lett*., 2010, **10**, 4975.
19 Y. Wang, Y. Zhao, D. W. Matson, J. Li and Y. Lin, *ACS Nano*, 2010, **4**, 1790.
20 D. Geng, Y. Chen, Y. chen, Y. Li, R. Li, X. Sun, S. Ye and S. Knight, *Energy Environ. Sci.*, 2011, **4**, 760.
21 C. Zhang, R. Hao, H. Liao and Y. Hou, *Nano Energy*, 2013, **2**, 88.
22 B. L. Allen, P. D. Kichambare and A. Star, *ACS Nano*, 2008, **2**, 1914.
23 J. Campos-Delgado, I. O. Maciel, D. Cullen, D. J. Smith, A. Jorio, M. A. Prmenta, H. Terrones and M. Terrones, *ACS Nano*, 2010, **4**, 1696.
24 F. Ma, H. Zhao, L. Sun, Q. Li, L. Huo, T. Xia, S. Gao, G. Pang, Z. Shi and S. Feng, *J. Mater. Chem.*, 2012, **22**, 13464.
25 C. H. Choi, S. H. Park and S. I. Woo, *J. Mater. Chem*. 2012, **22**, 12107.
26 C. Hu, Y. Xiao, Y. Zhao, N. Chen, Z. Zhang, M. Cao and L. Qu, *Nanoscale*,2013, **5**, 2726.
27 D. Bhattachariya, H.-Y. Park, M.-S. Kim, H.-S. Choi, S. N. Inamdar and J.-S. Yu, *Langmuir*, 2014, **30**, 318.
28 A. Watthanaphanit, G. Panomsuwan and N. Saito, *RSC adv*., 2014, **4**, 1622.
29 M. A. Bratescu, S.P. Cho, O. Takai and N. Saito, *J. Phys. Chem. C*, 2011, **115**, 24569.
30 G. Saito, S. Hosokai, M. Tsubota and T. Akiyama, *Cryst. Growth Des*., 2012, **1**, 2455.
31 A. Watthanaphanit and N. Saito, *Polym. Deg. Stab*., 2013, **5**, 1072.
32 T. Shirafuji, Y. Noguchi, T. Yamamoto, J. Hieda, N. Saito, O. Takai, A. Tsuchimoto, K. Nojima and Y. Okabe, *Jpn. J. Appl. Phys*., 2013, **52**, 125101.
33 J. Kang, O. L. Li and N. Saito, *Nanoscale*, 2013, **5**, 6874.
34 J. Senthilnathan, K. S. Rao and M. Yoshimura, *J. Mater. Chem. A*, 2014, **2**, 3332.
35 T. Ishizaki, S. Chiba, Y. Kaneko and G. Panomsuwan, *J. Mater. Chem. A*, 2014, 2014, **2**, 10589.
36 O. Takai, *Pure App. Chem.*, 2008, **80**, 2003.
37 T. Hagino, H. kondo, K. Ishikawa, H. Kano, M. Sekine and M. Hori, *Appl. Phys. Exp*., 2012, **5**, 035101.
38 F. Kroushawi, H. Latifi, S. H. Hosseini, M. Peysokhan, H. Nikbakht and Y. Silani, *Plasma Chem. Plasma Process*, 2012, **32**, 959.
39 T. A. Witten and L. M. Sander, *Phys. Rev. Lett*. 1981, **47**, 1400.
40 B.-S. Lee, S.-B. Son, J.-H. Seo, K.-M. Park, G. Lee, S.-H. Lee, K. H. Oh, J.-P. Ahn and W.-R. Yu, *Nanoscale*, 2013, **5**, 4790.
41 Z. Q. Li, C. J. Lu, Z. P. Xia, Y. Zhou, Z. Luo, *Carbon*, 2007, **45**, 1686.
42 A. Nieto-Márquez, R. Romero, A. Romero and J. L. Valverde, *J. Mater. Chem.*, 2011, **21**, 1664.
43 A. C. Ferrari and J. Robertson, *Phys. Rev. B.*, 2000, **61**, 14095.
44 M. S. Dresselhaus, A. Jorio, M. Hofmann, G. Dresselhaus and R. Saito, *Nano Lett.*, 2010, **10**, 751.
45 S. Chen, J. Duan, M. Jaroniec and S. Z. Qaio, *Adv. Mater*. 2014, **26**, 2925.
46 L. Lai, J. R. Potts, D. Zhan, L. Wang, C. K. Poh, C. Tang, H. Gong, Z. Shen, J. Lin and R. S. Ruoff, *Energy Environ. Sci*., 2012, **5**, 7936.
47 C. V. Rao, C. R. Cabera and Y. Ishikawa, *J. Phys. Chem. Lett*., 2010, **1**, 2622.
48 C. A. Hancock, A. L. Ong, P. R. Slater and J. R. Varcoe, *J. Mater. Chem. A*, 2014, **2**, 3047.
49 S. Treimer, A. Tang and D. C. Johnson, *Electroanalysis*, 2002, **14**, 165
50 R. Liu, D. Wu, X. Feng and K. Müllen, *Angew. Chem. Int. Ed*., 2010, **49**, 2565
51 H. Kim, K. Lee and S. I. Woo, Y. Jung, *Phys. Chem. Chem. Phys*., 2011, **13**, 17505.
52 R.-S. Zhong, Y.-H.Qin, D.-F. Niu, J.-W. Tian, X.-S. Zhang, X.-G. Zhou, S.-G. Sun and W.-K. Yuan, *J. Power Source*, 2013, **225**, 192
53 L. Zhang and Z. Xia, *J. Phys. Chem. C*, 2011, **115**, 11170.
54 S. S. Harilal, R. C. Issac, C. V. Bindhu, V. P. N. Nampoori and C. P. G. Vallabhan, *J. Phys. D: Appl. Phys*., 1997, **30**, 1703.
55 Y. Yamagata, A. Sharma, J. Narayan, R. M. Mayo, J. W. Newman and K. Ebihara, *J. Appl. Phys*., 1999, **86**, 4154.
56 Z. Bo, Y. Yang, J. Chen, K. Yu, J. Yan and K. Cen, *Nanoscale*, 2013, **5**, 5180
57 E. G. Wang, Z. G. Guo, J. Ma, M. M. Zhou, Y. K. Pu, S. Liu, G. Y. Zhang and D. Y. Zhong, *Carbon*, 2003, 41, 1827.
58 J. M. Stillahn and E. R. Fisher, *J. Phys. Chem. C*, 2009, **113**, 1963.
59 T. J. Wasowicz, A. Kivimäki, M. Coreno and M. Zubek, *J. Phys. B: At. Mol. Opt. Phys*., 2014, **47**, 055103.
60 N. R. Hore and D. K. Russell, *J. Chem. Soc., Perkin Trans*., 1998, **2**, 269.